Chapter 9
Weak Focusing Synchrotron

Abstract This Chapter introduces to the weak focusing synchrotron, and to the theoretical material needed for the simulation exercises. It begins with a brief reminder of the historical context, and continues with beam optics and acceleration techniques which the weak synchrotron principle and methods lean on. Regarding the latter, it relies on basic charged particle optics and acceleration concepts introduced in the previous Chapters, and further addresses the following aspects:
- fixed closed orbit,
- periodic structure,
- periodic motion stability,
- optical functions,
- synchrotron motion,
- depolarizing resonances.

The simulation of weak synchrotrons only require a very limited number of optical elements; actually two are enough: DIPOLE or BEND to simulate combined function dipoles, and DRIFT to simulate straight section. A third one CAVITE, is required for acceleration. Particle monitoring requires keywords introduced in the previous Chapters, including FAISCEAU, FAISTORE, possibly PICKUPS, and some others. Spin motion computation and monitoring resort to SPNTRK, SPNPRT, FAISTORE. Optics matching and optimization use FIT[2]. SYSTEM again is used to shorten the input data files.

Notations used in the Text

B; **B**, $B_{x,y,s}$	field value; field vector, its components in the moving frame
$B\rho = p/q$; $B\rho_0$	particle rigidity; reference rigidity
C; C_0	orbit length, $C = 2\pi R + \left[\begin{smallmatrix}\text{straight}\\ \text{sections}\end{smallmatrix}\right.$; reference, $C_0 = C(p = p_0)$
E	particle energy
EFB	Effective Field Boundary
f_{rev}, f_{rf}	revolution and accelerating voltage frequencies
h	RF harmonic number, $h = f_{\text{rf}}/f_{\text{rev}}$
m; m_0; M	mass, $m = \gamma m_0$; rest mass; in units of MeV/c^2
$n = \frac{\rho}{B}\frac{dB}{d\rho}$	focusing index
p; p; p_0	momentum vector; its modulus; reference
$P_i,\ P_f$	polarization, initial, final
q	particle charge
$r,\ R$	orbital radius ; average radius, $R = C/2\pi$
s	path variable
v	particle velocity
$V(t);\ \hat{V}$	oscillating voltage; its peak value
x, x', y, y'	horizontal and vertical coordinates in the moving frame

α	momentum compaction
α	trajectory angle
$\beta = v/c$; β_0; β_s	normalized particle velocity; reference; synchronous
β_u	betatron functions ($u:\ x, y, Y, Z$)
$\gamma = E/m_0$	Lorentz relativistic factor
δp	momentum offset or Dirac distribution
Δp	momentum offset
ε	wedge angle
ε_u	Courant-Snyder invariant ($u:\ x, r, y, l, Y, Z, s$, etc.)
ϵ_R	strength of a depolarizing resonance
μ_{u}	betatron phase advance, $\mu_{\text{u}} = \int_{\text{period}} ds/\beta_u(s)$ ($u:\ x, y, Y, Z$)
ν_{u}	wave number or "tune", radial, vertical, synchrotron ($u:\ x, y, Y, Z, l$)
$\rho,\ \rho_0$	curvature radius; reference
σ	beam matrix
$\phi;\ \phi_s$	particle phase at voltage gap; synchronous phase
ϕ_u	betatron phase advance, $\phi_u = \int ds/\beta_u$ ($u:\ x, y, Y, orZ$)
φ	spin angle to the vertical axis

Introduction

The synchrotron is an outcome of the mid-1940s longitudinal phase focusing synchronous acceleration concept [1, 2]. In its early version, transverse beam stability in the synchrotron during the thousands of turns that the acceleration lasts was based on the technique known at the time: weak focusing, as in the cyclotron and in the betatron. An existing betatron was used to first demonstrate phase-stable synchronous acceleration with slow variation of the magnetic field, on a fixed orbit, in 1946 [3], - closely following the demonstration of the principle of phase focusing using a fixed-field cyclotron [4].

Phase focusing states that stability of the longitudinal motion, longitudinal focusing, is obtained if particles in a bunch, which have a natural energy spread, arrive at the accelerating gap in the vicinity of a proper phase of the oscillating voltage, the synchronous phase; if this condition is fulfilled the bunch stays together, in the vicinity of the latter, during acceleration. Synchrotrons operate in general in a non-isochronous regime: the revolution period changes with energy; as a consequence, in order to maintain an accelerated bunch on the synchronous phase, the RF voltage frequency, which satisfies $f_{\mathrm{rf}} = hf_{\mathrm{rev}}$, has to change continuously from injection to top energy. The reference orbit in a synchrotron is maintained at constant radius by ramping the guiding field in the main dipoles in synchronism with the acceleration, as in the betatron [5].

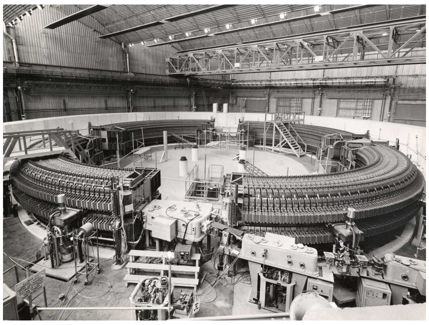

Fig. 9.1 SATURNE I at Saclay [6], a 3 GeV, 4-period, 68.9 m circumference, weak focusing synchrotron, constructed in 1956-58. The injection line can be seen in the foreground, injection is from a 3.6 MeV Van de Graaff (not visible)

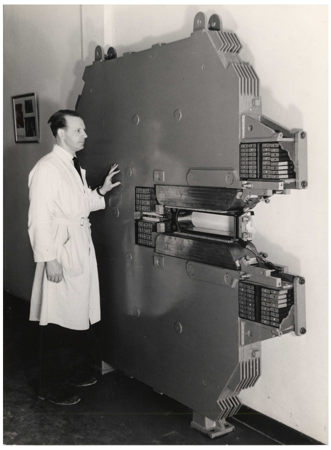

Fig. 9.2 A slice of SATURNE I dipole [6]. The slight gap tapering is hardly visible (increasing outward), it determines the weak index condition $0 < n < 1$

The synchrotron concept allowed the highest energy reach by particle accelerators at the time, it led to the construction of a series of proton rings with increasing energy [7]: 1 GeV at Birmingham (1953), 3.3 GeV at the Cosmotron (Brookhaven National Laboratory, 1953-1969), 6.2 GeV at the Bevatron (Berkeley, 1954-1993), 10 GeV at the Synchro-Phasotron (JINR, Dubna, 1957-2003), and a few additional ones in the late 1950s well into the era of the concept which would essentially dethrone the weak focusing method and its quite bulky rings of magnets which were a practical limit to further increase in energy[1]: the strong focusing synchrotron (the object of Chapter 10). The general layout of these first weak focusing synchrotrons included straight sections (often 4, Fig. 9.1), which allowed insertion of injection (Fig. 9.1) and extraction systems, accelerating cavities, orbit correction and beam monitoring equipment.

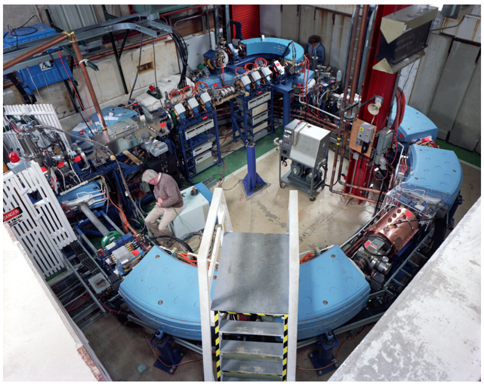

Fig. 9.3 Left: Loma Linda University medical synchrotron [8], during commissioning in 1989 at the Fermilab National Laboratory where it was designed

The next decades following the invention of the synchrotron saw applications in many fields of science including fixed-target nuclear physics for particle discovery, material science, medicine, industry. Its technological simplicity still makes it an appropriate technology today in low energy beam application when relatively low current is not a concern, as in the hadrontherapy application (Fig. 9.3) [9, 10]: it essentially requires a single type of a simple dipole magnet, an accelerating gap, some command-control instrumentation, whereas it procures greater beam manipulation flexibilities compared to (synchro-)cyclotrons.

Polarized beams

The availability of polarized proton sources allowed the acceleration of polarized beams to high energy. The possibility was considered from the early times at Argonne ZGS (Zero-Gradient Synchrotron), a 12 GeV weak focusing synchrotron operated over 1964-1979 [11] (Fig. 9.4). Up to 70% polarization transmission through the synchrotron was achieved, for the first time in a synchrotron[2] and reaching multi-GeV energy in 1973, up to 17.5 GeV/c with *appreciable polarizations* [12]. Polarization preservation techniques included harmonic orbit correction and fast betatron tune jump at strongest depolarizing resonances [13] (Fig. 9.16). Experiments were performed to assess the possibility of polarization transmission in strong focusing

[1] The story has it that it is possible to ride a bicycle in the vacuum chamber of Dubna's Synchro-Phasotron.

[2] Polarized beam had been accelerated in cyclotrons, at earlier times.

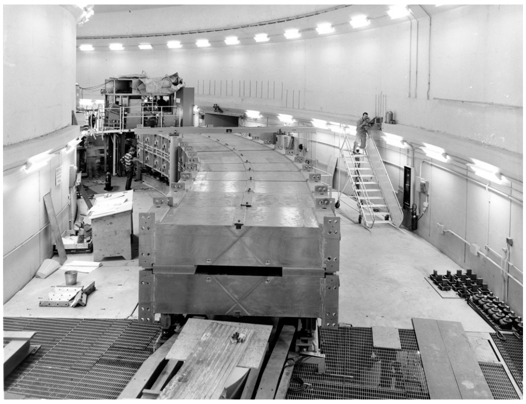

Fig. 9.4 The ZGS at Argonne during construction. A 12 GeV, 8-dipole, 4-period, 172 m circumference, wedge focusing synchrotron. The two persons inside and outside the ring, in the background, give an idea of the size of the magnets

synchrotrons, and polarization lifetime in colliders [14]. Acceleration of polarized deuteron was achieved in the late 1970s, when sources where made available [15].

9.1 Basic Concepts and Formulæ

The synchrotron is based on two key principles. On the one hand, a slowly varying magnetic field to maintain a constant orbit during acceleration,

$$B(t) \times \rho = p(t)/q, \quad \rho = constant, \tag{9.1}$$

with $p(t)$ the particle momentum and ρ the bending radius in the dipoles. On the other hand, on synchronous acceleration for longitudinal phase stability. In a regime where the velocity change with energy cannot be ignored (non-ultrarelativistic particles), the latter requires a modulation of the accelerating voltage frequency so to satisfy

$$f_{\mathrm{rf}}(t) = h f_{\mathrm{rev}}(t) \tag{9.2}$$

Synchronism between accelerating voltage oscillation and the revolution motion keeps the bunch on the synchronous phase at traversal of the accelerating gaps. Synchronous acceleration is technologically simpler in the case of electrons, as frequency modulation is unnecessary beyond a few MeV; for instance, from $v/c = 0.9987$ at 10 MeV to $v/c \rightarrow 1$ the relative change in revolution frequency amounts to $\delta f_{\mathrm{rev}}/f_{\mathrm{rev}} = \delta\beta/\beta < 0.0013$.

These are two major evolutions compared to the cyclotron, where, instead, the magnetic field is fixed - the reference orbit spirals out, and, by virtue of the isochronism of the orbits, the oscillating voltage frequency is fixed as well.

A fixed orbit reduces the radial extent of individual guiding magnets, allowing a ring structure comprised of a circular string of dipoles. For the sake of comparison: a synchrocyclotron instead uses a single, massive dipole; increased energy requires increased radial extent of the magnet to allow for the greater bending field integral (*i.e.*, $\oint B\,dl = 2\pi R_{max}\hat{B} = p_{max}/q$), thus a volume of iron increasing more than quadratically with bunch rigidity.

One or the other of the weak index ($-1 < k < 0$, Sect. 4.2.2) and/or wedge focusing (Sect. 15.3.1) are used in weak focusing synchrotrons. Transverse stability was based on the latter at Argonne ZGS (Zero-Gradient Synchrotron: the main magnet had no field index); ZGS accelerated polarized proton beams, weak focusing resulted in weak depolarizing resonances, an advantage in that matter [14].

Due to the necessary ramping of the field, and of the RF frequency to follow, in order to maintain a constant orbit, the synchrotron is a pulsed accelerator, the acceleration is cycled, from injection to top energy, repeatedly. The repetition rate of the acceleration cycle depends on the type of power supply. If the ramping uses a constant electromotive force (E=V+Z I is constant), then

$$B(t) \propto (1 - e^{-\frac{t}{\tau}}) = 1 - \left[1 - \left(\frac{t}{\tau}\right) + \left(\frac{t}{\tau}\right)^2 - \ldots\right] \approx \frac{t}{\tau} \tag{9.3}$$

essentially linear; $\dot{B} = dB/dt$ does not exceed a few Tesla/second: the repetition rate of the acceleration cycle if of the order of a Hertz. If instead the magnet winding is part of a resonant circuit then the field oscillates from an injection threshold to a maximum value, $B(t) : B_0 \longrightarrow B_0 + \hat{B}$, as in the betatron; the repetition rate is up to a few tens of Hertz. In both cases anyway B imposes its law and the other quantities comprising the acceleration cycle (RF frequency in particular) will follow B(t).

For the sake of comparison: in a synchrocyclotron the field is constant, thus acceleration can be cycled as fast as the swing of the voltage frequency allows (hundreds of Hz are common practice); assume a conservative 10 kVolts per turn, thus of the order of 10,000 turns to 100 MeV, with velocity $0.046 < v/c < 0.43$ from 1 to 100 MeV, proton. Take $v \approx 0.5c$ to make it simple, an orbit circumference below 30 meter, thus the acceleration takes of the order of $10^4 \times C/0.5c$ ≈ms range, potentially a repetition rate in kHz range, more than an order of magnitude beyond the reach of a rapid-cycling pulsed synchrotron.

9.1.1 Periodic Stability

This section introduces the various components of the transverse focusing and the conditions for periodic stability in a weak focusing synchrotron. It builds on material introduced in Chap. 4, Classical Cyclotron.

9.1.1.1 Closed orbit

The concept is found in the betatron, which accelerates particles on a constant orbit (Chap. 7). The closed orbit is fixed, and maintained during acceleration by ensuring that the relationship Eq. 9.1 is satisfied. In a perfect ring, the closed orbit is along an arc in the bending magnets and straight along the drifts, Fig. 9.5.

Particle motion is defined in a moving frame (O;s,x,y) whose origin coincides with the location of an ideal particle following the reference orbit. The moving frame s axis is tangent to the reference orbit, its transverse horizontal axis x is normal to the s axis, its vertical axis y is normal to the (s, x) plane (Fig. 4.8, Sect. 4.2.2).

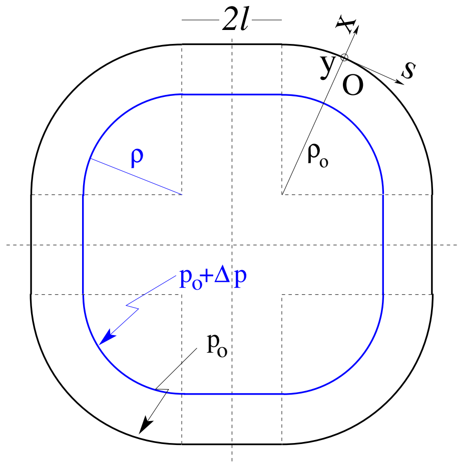

Fig. 9.5 A $2\pi/4$ axially symmetric structure with four drift spaces. Orbit length on reference momentum p_0 is $C = 2\pi\rho_0 + 8l$. (O;s,x,y) is the moving frame, along the reference orbit. The orbit for momentum $p = p_0 + \Delta p$ ($\Delta p < 0$, here) is at constant distance $\Delta x = \frac{\rho_0}{1-n}\frac{\Delta p}{p_0} = \frac{R}{(1+k)(1-n)}\frac{\Delta p}{p_0}$ from the reference orbit

9.1.1.2 Transverse Focusing

Radial motion stability around a reference closed orbit in an axially symmetric dipole field requires a field index (Sect. 4.2.2),

$$n = -\frac{\rho_0}{B_0}\frac{\partial B_y}{\partial x}\bigg|_{\mathrm{x=0,\ y=0}} \tag{9.4}$$

a quantity evaluated on the reference arc in the dipoles, satisfying the weak focusing condition (Eq. 4.11 with $n = -k$)

$$0 < n < 1 \tag{9.5}$$

This condition can be obtained with a tapered gap (as in SATURNE dipoles, Fig. 9.2) causing the magnetic field to decrease slowly with radius, so resulting in both axial and radial focusing (Figs. 9.6, 9.7). Note the sign convention here, the cyclotron uses the opposite sign (Eq. 4.10). This condition holds regardless of the presence of drifts or not. Adding drift spaces between the dipoles, the reference orbit is comprised of arcs of radius ρ_0 in the magnets, and straight segments along the drift spaces that connect these arcs. This requires defining two radii, namely,

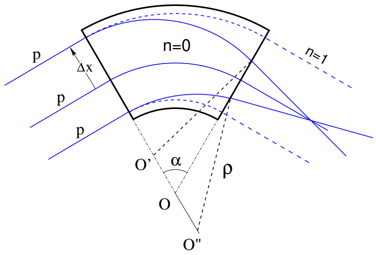

Fig. 9.6 Geometrical focusing: in a sector dipole with focusing index $n = 0$, parallel incoming rays of equal momenta experience the same curvature radius ρ, their trajectories converge as outer trajectories have a longer path in the field, inner ones shorter. An index value n=1 cancels that effect: parallel incoming rays exit parallel

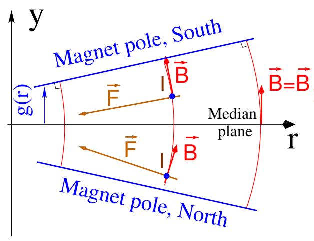

Fig. 9.7 Axial motion stability requires proper shaping of field lines: B_y has to decrease with radius. The Laplace force pulls a positive charge with velocity pointing out of the page, at I, toward the median plane. Increasing the field gradient (n closer to 1, gap opening up faster) increases the focusing

(i) the magnet curvature radius ρ_0,

(ii) an average radius $R = C/2\pi = \rho_0 + Nl/\pi$ (with C the length of the reference closed orbit and $2l$ the drift length) (Fig. 9.5) which also writes

$$R = \rho_0(1+k), \qquad k = \frac{Nl}{\pi\rho_0} \tag{9.6}$$

Adding drift spaces decreases the average focusing around the ring.

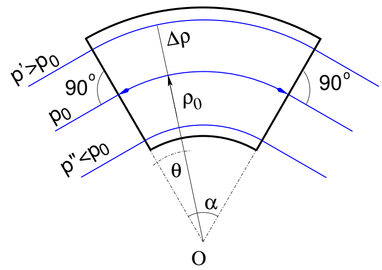

Fig. 9.8 In a sector dipole with radial index $n \neq 0$, closed orbits follow arcs of constant field. A closed orbit at $p_0 + \Delta p$ follows an arc of radius $\rho_0 + \Delta\rho$, $\Delta\rho = \Delta p/(1+n)qB_0$

Geometrical focusing

The limit $n \to 1$ of the transverse motion stability domain corresponds to a cancellation of the geometrical focusing (Fig. 9.6): in a constant field dipole (radial field index n=0) the longer (respectively shorter) path in the magnetic field for parallel trajectories entering the magnet at greater (respectively smaller) radius result in convergence. This effect is cancelled, *i.e.*, trajectory angle is the same whatever the entrance radius, if the curvature center is made independent of the entrance radius: $OO' = 0$, $O''O = 0$. This occurs if trajectories at an outer (inner) radius experience a smaller (greater) field such as to satisfy $BL = B\rho\,\alpha = C^{st}$. Differentiating $B\rho = C^{st}$ gives $\frac{\Delta B}{B} + \frac{\Delta\rho}{\rho} = 0$, with $\Delta\rho = \Delta x$, so yielding $n = -\frac{\rho_0}{B_0}\frac{\Delta B}{\Delta x} = 1$. The focal distance associated with the curvature is (Eq. 4.12 with $R = \rho_0$) $f = \frac{\rho_0^2}{\mathcal{L}}$. Optical drawbacks of the weak focusing method include the weakness of the focusing and the absence of independent radial and axial focusing.

Wedge Focusing

Entrance and exit wedge angles may be used to ensure transverse focusing, Fig. 9.9: opening the magnetic sector increases the horizontal focusing (and decreases the vertical focusing); closing the magnetic sector has the reverse effect (see Sect. 15.3.1).

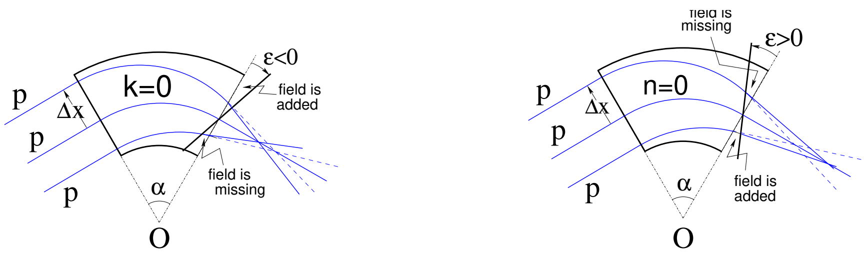

Fig. 9.9 Left: a focusing wedge ($\varepsilon < 0$); opening the sector increases horizontal focusing and decreases vertical focusing. Right: a defocusing wedge ($\varepsilon > 0$), closing the sector, has the reverse effect. This is the origin of the focusing in the ZGS zero-gradient dipoles

In a point transform approximation, at the wedge the trajectory undergoes a local deviation proportional to the distance to the optical axis, amounting to

$$\Delta x' = \frac{\tan\varepsilon}{\rho_0}\Delta x, \quad \Delta y' = -\frac{\tan(\varepsilon - \psi)}{\rho_0}\Delta y \tag{9.7}$$

The ψ angle component is a correction for the fringe field extent (Eq. 15.21); the effect of the latter, of the first order on the vertical focusing, is of second order horizontally.

Profiling the magnet gap in order to adjust the focal distance complicates the magnet; a parallel gap, $n = 0$, makes it simpler, for that reason edge focusing may be preferred. Wedge vertical focusing in the ZGS ($\varepsilon > 0$) was at the expense of horizontal geometrical focusing (Fig. 9.6). This was an advantage though, for the acceleration of polarized beams, as radial field components (which are responsible for depolarization) were only met at the EFBs of the eight main dipoles, and weak [12]. Preserving beam polarization at high energy required tight control of the tunes, this was achieved by pole face windings added at the ends of the dipoles [17, 18], pulsed to control the amplitude detuning, resulting in a control of the tunes at 0.01 level.

9.1.1.3 Betatron motion

The first order differential equations of motion in the moving frame (Fig. 9.5) derive from the Lorentz equation

$$\frac{dm\mathbf{v}}{dt} = q\mathbf{v}\times\mathbf{B} \ \Rightarrow\ m\frac{d}{dt}\left\{\begin{matrix}\frac{ds}{dt}\mathbf{s}\\ \frac{dx}{dt}\mathbf{x}\\ \frac{dy}{dt}\mathbf{y}\end{matrix}\right\} = q\left\{\begin{matrix}\left(\frac{dx}{dt}B_y - \frac{dy}{dt}B_x\right)\mathbf{s}\\ -\frac{ds}{dt}B_y\mathbf{x}\\ \frac{ds}{dt}B_x\mathbf{y}\end{matrix}\right\} \tag{9.8}$$

Motion in a weak index dipole field is solved in Sect. 4.2.2, Classical Cyclotron: in the latter substitute ρ to R, $n = -\frac{\rho_0}{B_0}\frac{\partial B_y}{\partial x}$ to $-k$, evaluated on the reference orbit. Taylor expansions of the transverse field components in the moving frame (Eq. 4.6) lead to

$$\begin{aligned}B_y(\rho)|_{\mathrm{y}=0} &= B_0(1-n\tfrac{x}{\rho_0}) + O(x^2)\\ B_x(0+y) &= -n\tfrac{B_0}{\rho_0}y + O(y^3)\end{aligned} \tag{9.9}$$

Assume transverse stability: $0 < n < 1$; in the approximation $ds \approx vdt$ (Eq. 4.13) Eqs. 9.8, 9.9 lead to the differential equations of motion

$$\frac{d^2x}{ds^2} + \frac{1-n}{\rho_0^2}x = 0, \qquad \frac{d^2y}{ds^2} + \frac{n}{\rho_0^2}y = 0 \tag{9.10}$$

It results that, in an S-periodic structure comprised of gradient dipoles, wedges and drift spaces, the differential equation of motion takes the general form of Hill's equation, a second order differential equation with periodic coefficient, namely (with u standing for x or y),

$$\left\{\begin{aligned}&\frac{d^2u}{ds^2} + K_u(s)u = 0\\ &K_u(s+S) = K_u(s)\end{aligned}\right. \quad \text{with} \left\{\begin{aligned}&\text{in dipoles : }\left\{\begin{aligned}K_x &= \tfrac{1-n}{\rho_0^2}\\ K_y &= \tfrac{n}{\rho_0^2}\end{aligned}\right.\\ &\text{at a wedge at } s=s_0 :\ K_{\substack{x\\y}} = \tfrac{\pm\tan\varepsilon}{\rho_0}\delta(s-s_0)\\ &\text{in drift spaces : } \tfrac{1}{\rho_0} = 0,\ K_x = K_y = 0\end{aligned}\right. \tag{9.11}$$

$K_u(s)$ is S-periodic, $S = 2\pi R/N$ ($S = C/4$ for instance in a 4-periodic ring, Figs. 9.1, 9.5).

The solution of Eqs. 9.11 is not as straightforward as in the cyclotron where K_u is constant around the ring (Eq. 4.14), which results in a sinusoidal motion (Eq. 4.16) - the latter is on the other hand a reasonable approximation, see below, *Weak focusing approximation*. G. Floquet has established [19] that the two independent solutions of Hill's second order differential equation have the form [16]

$$\left| \begin{array}{l} u_1(s) = \sqrt{\beta_u(s)}\, e^{\,i\int_0^s \frac{ds}{\beta_u(s)}} \\ du_1(s)/ds = \dfrac{i - \alpha_u(s)}{\beta_u(s)}\, u_1(s) \end{array} \right. \quad \text{and} \quad \left| \begin{array}{l} u_2(s) = u_1^*(s) \\ du_2(s)/ds = du_1^*(s)/ds \end{array} \right. \tag{9.12}$$

wherein $\beta_u(s)$ and $\alpha_u(s) = -\beta_u'(s)/2$ are S-periodic functions, from what it results that

$$u_{\frac{1}{2}}(s + S) = u_{\frac{1}{2}}(s)\, e^{\pm i\mu_u} \tag{9.13}$$

wherein

$$\mu_u = \int_{s_0}^{s} \frac{ds}{\beta_u(s)} \tag{9.14}$$

is the betatron phase advance at s, from the origin s_0. A real solution of Hill's equation is the linear combination $A\, u_1(s) \; + \; A^*\, u_2^*(s)$. With $A \; = \; \frac{1}{2}\sqrt{\varepsilon_u/\pi}e^{i\phi}$ following conventional notations, ϕ the phase of the motion at the origin $s = s_0$, the general solution of Eq. 9.11 writes

$$\left| \begin{array}{l} u(s) = \sqrt{\beta_u(s)\varepsilon_u/\pi}\, \cos\left(\int_{s_0}^{s} \dfrac{ds}{\beta_u} + \phi\right) \\ u'(s) = -\sqrt{\dfrac{\varepsilon_u/\pi}{\beta_u(s)}}\, \sin\left(\int_{s_0}^{s} \dfrac{ds}{\beta_u} + \phi\right) + \alpha_u(s)\, \cos\left(\int_{s_0}^{s} \dfrac{ds}{\beta_u} + \phi\right) \end{array} \right. \tag{9.15}$$

An invariant of the motion, known as the Courant-Snyder invariant, is

$$\frac{1}{\beta_u(s)}\left[u^2 + (\alpha_u(s)u + \beta_u(s)u')^2\right] = \frac{\varepsilon_u}{\pi} \tag{9.16}$$

At a given azimuth s of the periodic structure the observed turn-by-turn motion lies on that ellipse (Fig. 9.10). The form and inclination of the ellipse depend on the observation azimuth s via the respective local values of $\alpha_u(s)$ and $\beta_u(s)$, but its surface ε_u is invariant. Motion along the ellipse is clockwise, as can be figured from Eq. 9.15 considering an observation azimuth s where the ellipse is upright, $\alpha_u(s) = 0$. The phase advance over a turn (from one position to the next on the ellipse, Fig. 9.10) in an N-periodic ring yields the wave number

$$\nu_u = N\mu_u = \int_{s_0}^{s_0+NS} \frac{ds}{\beta_u(s)} = N\int_{\text{period}} \frac{ds}{\beta_u(s)} \tag{9.17}$$

Weak focusing approximation

In a cylindrically symmetric structure a sinusoidal motion is the exact solution of the first order differential equations of motion (Eqs. 4.15, 4.16, Classical Cyclotron Chapter), the coefficients $K_x = (1 - n)/R_0^2$ and $K_y = n/R_0^2$ are constant (s-independent). Adding drift spaces results in Hill's differential equation with periodic coefficient $K(s+S) = K(s)$ (Eq. 9.11), and in a pseudo harmonic solution (Eq. 9.15). Due to the

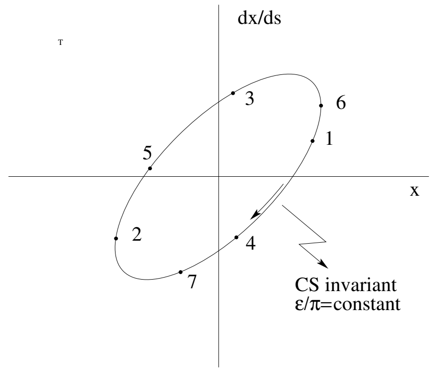

Fig. 9.10 Courant-Snyder invariant and turn-by-turn harmonic motion along the invariant, observed at some azimuth s. The form and tilt-angle of the ellipse depend on the observation azimuth s but its surface ε_u is invariant

weak focusing the beam envelope is only weakly modulated (see below), thus so is $\beta_u(s)$. In a practical manner, the modulation of $\beta_u(s)$ does not exceed a few percent, this justifies introducing the average value $\overline{\beta_u}$ to approximate the phase advance by

$$\int_0^s \frac{ds}{\beta_u(s)} \approx \frac{s}{\overline{\beta_u}} = \nu_u \frac{s}{R} \tag{9.18}$$

The right equality is obtained by applying this approximation to the phase advance per period, namely (Eq. 9.14) $\mu_u = \int_{s_0}^{s_0+S} \dfrac{ds}{\beta_u(s)} \approx S/\overline{\beta_u}$, and introducing the wave number of the N-period optical structure $\nu_u = \frac{N\mu_u}{2\pi} = \frac{\text{phase advance over a turn}}{2\pi}$ so that

$$\overline{\beta_u} = \frac{R}{\nu_u} \tag{9.19}$$

the wavelength of the betatron oscillation around the ring. With $k \ll 1$ and using Eq. 9.23,

$$\overline{\beta_x} = \frac{\rho_0(1+k/2)}{\sqrt{1-n}}, \quad \overline{\beta_y} = \frac{\rho_0(1+k/2)}{\sqrt{n}} \tag{9.20}$$

Substituting $\nu_u \frac{s}{R}$ to $\int \frac{ds}{\beta_u(s)}$ in Eq. 9.15 yields the approximate solution

$$\left| \begin{array}{l} u(s) \approx \sqrt{\beta_u(s)\varepsilon_u/\pi}\, \cos\left(\nu_u \dfrac{s}{R} + \phi\right) \\ u'(s) \approx -\sqrt{\dfrac{\varepsilon_u/\pi}{\beta_u(s)}}\, \sin\left(\nu_u \dfrac{s}{R} + \phi\right) + \alpha_u(s)\, \cos\left(\nu_u \dfrac{s}{R} + \phi\right) \end{array} \right. \tag{9.21}$$

Beam envelopes

The beam envelope $\hat{u}(s)$ (with u standing for x or y) is determined by the particle of maximum invariant ε_u/π, it is given at all s by

$$\hat{u}_{\text{env}}(s) = \pm\sqrt{\beta_u(s)\frac{\varepsilon_u}{\pi}} \tag{9.22}$$

As $\beta_u(s)$ is S-periodic, so is the envelope, $\hat{u}(s+S) = \hat{u}(s)$. In a cell with symmetries,

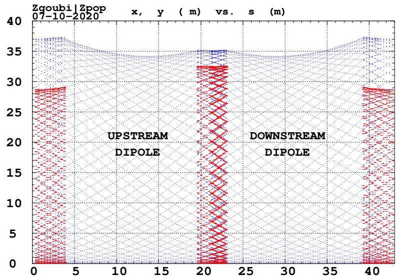

Fig. 9.11 Multi-turn particle excursion along the ZGS 2-dipole 43 m cell. The motion extrema (Eq. 9.22) tangent the envelops, respectively horizontal (red), and vertical (blue). Envelops have the symmetry of the cell

beam envelops feature the same symmetries, as in Fig. 9.11 for instance: a symmetry with respect to the center of the cell; envelop extrema are at azimuth s of $\beta_u(s)$ extrema, *i.e.* where $d\hat{u}(s)/ds \propto \beta'_u(s) = 0$ or $\alpha_u = 0$ as $\beta'_u = -2\alpha_u$.

Working point

The "working point" of the synchrotron is the wave number couple (ν_x, ν_y) at which the accelerator is operated, it fully characterizes the focusing. In a structure with cylindrical symmetry (such as the Classical Cyclotron) $\nu_x = \sqrt{1-n}$ and $\nu_y = \sqrt{n}$ (Eq. 4.17) so that $\nu_x^2 + \nu_y^2 = 1$: when the radial field index n is changed the working point stays on a circle of radius 1 in the stability diagram (or "tune diagram", Fig. 9.12). If drift spaces are added, from Eqs. 9.19, 9.20, with $1 + \frac{k}{2} \approx \sqrt{R/\rho_0}$ (Eq. 9.6), it comes

$$\nu_x \approx \sqrt{(1-n)\frac{R}{\rho_0}}, \quad \nu_y \approx \sqrt{n\frac{R}{\rho_0}}, \qquad \nu_x^2 + \nu_y^2 \approx \frac{R}{\rho_0} \tag{9.23}$$

thus the working point is located on the circle of radius $\sqrt{R/\rho_0} > 1$ (Fig. 9.12). Tunes can not exceed the limits

$$0 < \nu_{\text{x, y}} \lesssim \sqrt{R/\rho_0}$$

Horizontal and vertical focusing are not independent (Eq. 9.11): if ν_x increases then ν_y decreases and reciprocally. This is a lack of flexibility which the advent of strong focusing will overcome by providing two knobs allowing separate adjustment of the tunes.

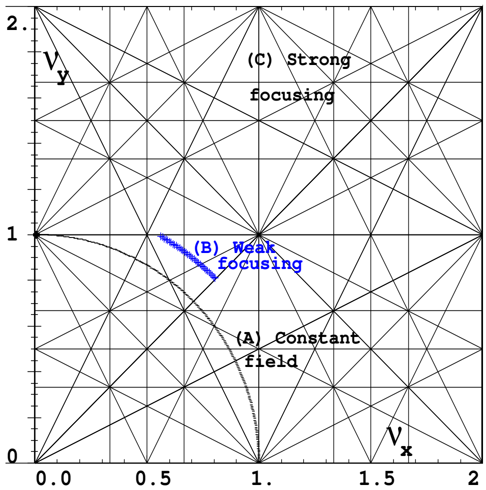

Fig. 9.12 Location of the working point in the tune diagram. (A) field with revolution symmetry: (ν_x, ν_y) is on a circle of radius 1; (B) sector field with field index $0 < n < 1$ and drift spaces: (ν_x, ν_y) is on a circle of radius $(\sqrt{R/\rho_0})$; (C) strong focusing, field index $|n| \gg 1$, ν_x and ν_y are independent and large

Off-momentum orbits; *periodic dispersion*

In the linear approximation in $\Delta p/p_0$, a momentum offset $\Delta p = p - p_0$ changes mv to $mv(1 + \Delta p/p_0)$ in Eq. 9.8; this changes the horizontal equation of motion (Eq. 9.10) to

$$\frac{d^2x}{ds^2} + K_x x = \frac{1}{\rho_0}\frac{\Delta p}{p_0}, \quad \text{or} \quad \frac{d^2x}{ds^2} + K_x\left(x - \frac{1}{\rho_0 K_x}\frac{\Delta p}{p_0}\right) = 0 \tag{9.24}$$

A change of variable $x - \frac{1}{K_x\rho_0}\frac{\Delta p}{p_0} \rightarrow x$ (with $1/\rho_0 K_x = \rho_0/(1-n)$) restores the unperturbed equation of motion; thus orbits of different momenta $p = p_0 + \Delta p$ are distant

$$\Delta x = \frac{\rho_0}{1-n}\frac{\Delta p}{p_0} \tag{9.25}$$

from the reference orbit (Fig. 9.8). Introduce the geometrical radius $R = (1+k)\rho_0$ (Eq. 9.6) to account for the added drifts; this yields the dispersion function

$$D_x = \frac{\Delta x}{\Delta p/p_0} \equiv \frac{\Delta R}{\Delta p/p_0} = \frac{R}{(1-n)(1+k)} = \frac{\rho_0}{1-n}, \quad \text{constant, positive} \tag{9.26}$$

D_x is the chromatic dispersion of the orbits, an s-independent quantity: in a structure with axial symmetry, comprising drift sections (Fig. 9.5) or not (classical and AVF cyclotrons for instance), the ratio $\frac{\Delta x}{\rho_0 \Delta p/p_0}$ is independent of the azimuth s, the distance of a chromatic orbit to the reference orbit is constant around the ring.

Given that $n < 1$,

- higher momentum orbits, $p > p_0$, have a greater radius,
- lower momentum orbits, $p < p_0$, have a smaller radius.

The horizontal motion of an off-momentum particle is a superposition of the betatron motion (solution of Hill's Eq. 9.21 with $\delta p/p = 0$) and of a particular solution of the inhomogeneous equation ($\delta p/p \neq 0$), namely

$$x(s) = \sqrt{\beta_u(s)\varepsilon_u/\pi}\,\cos\left(\nu_u \frac{s}{R} + \phi\right) + \frac{\rho_0}{1-n}\frac{\Delta p}{p_0} \tag{9.27}$$

whereas the vertical motion is unchanged.

Chromatic orbit length

In an axially symmetric structure the difference in closed orbit length $\Delta C = 2\pi\Delta R$ resulting from the difference in momentum arises in the dipoles, as all orbits are parallel in the drifts (Fig. 9.5). Hence, from Eq. 9.26, the relative closed orbit lengthening factor, or momentum compaction

$$\alpha = \frac{\Delta C}{C}\Big/\frac{\Delta p}{p_0} \equiv \frac{\Delta R}{R}\Big/\frac{\Delta p}{p_0} = \frac{1}{(1-n)(1+k)} \approx \frac{1}{\nu_x^2} \tag{9.28}$$

with $k = Nl/\pi\rho_0$ (Eq. 9.6). Note that the relationship $\alpha \approx 1/\nu_x^2$ between momentum compaction and horizontal wave number established for a revolution symmetry structure (Eq. 4.21) still holds when adding drifts.

9.1.2 Longitudinal Motion

In a synchrotron, the field B is varied during acceleration (a function performed by the magnet power supply) concurrently with the variation of the bunch momentum p (a function performed by the accelerating cavity) in such a way that the beam is maintained on the design orbit. Given the energies involved, the magnet supply imposes its law $B(t)$ (Fig. 9.13) and the cavity follows, the best it can. The accelerating voltage $\hat{V}(t) = \sin\omega_{\mathrm{rf}}t$ is maintained in synchronism with the revolution motion, its angular frequency satisfying

$$\omega_{\mathrm{rf}} = h\omega_{\mathrm{rev}} = h\frac{c}{R}\frac{B(t)}{\sqrt{\left(\frac{m_0}{q\rho}\right)^2 + B^2(t)}}$$

Energy gain

The variation of the particle energy over a turn amounts to the work of the force $F = dp/dt = q\rho dB/dt$ on the charge at the cavity, namely

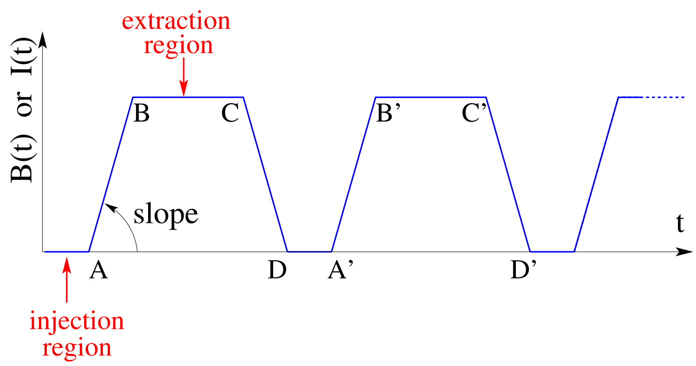

Fig. 9.13 Cycling $B(t)$ in a pulsed synchrotron. Ignoring saturation, $B(t)$ is proportional to the magnet power supply current $I(t)$. Beam injection occurs at low field, in the region of A, extraction occurs at top energy, on the high field plateau. (AB): field ramp up (acceleration); (BC): flat top; (CD): field ramp down; (DA'): thermal relaxation. (AA'): repetition period; (1/AA'): repetition rate; *slope*: ramp velocity $\dot{B} = dB/dt$ (Tesla/s).

$$\Delta W = F \times 2\pi R = 2\pi R q \rho \dot{B} \tag{9.29}$$

Over most of the acceleration cycle in a slow-cycling synchrotron $\dot{B}$ is usually constant (Eq. 9.3), thus so is ΔW. At SATURNE I for instance (the object of Exercise 9.1, parameters in Tab. 9.1)

$$\frac{\Delta W}{q} = 2\pi R \rho \dot{B} = 68.9 \times 8.42 \times 1.8 = 1044 \text{ volts}$$

The field ramp lasts

$$\Delta t = (B_{\max} - B_{\min})/\dot{B} \approx B_{\max}/\dot{B} = 0.8\,\text{s}$$

The number of turns to the top energy ($W_{\max} \approx 3$ GeV) is

$$N = \frac{W_{\max}}{\Delta W} = \frac{3\,10^9 \text{ eV}}{1044 \text{ eV/turn}} \approx 3\,10^6 \text{turns}$$

The dependence of particle mass on field writes

$$m(t) = \gamma(t) m_0 = \frac{q\rho}{c}\sqrt{\left(\frac{m_0}{qc\rho}\right)^2 + B(t)^2}$$

2191 *Adiabatic damping of the betatron oscillations*

The focusing index (Eq. 9.4) does not change during acceleration, thus the tunes ν_x and ν_y do not change either. As a result of the longitudinal acceleration at the cavity though, the longitudinal energy of the particles is modified. This results in a decrease of the amplitude of betatron oscillations (an increase if the cavity is decelerating). The mechanism is sketched in Fig. 9.14: the slope, respectively before and after (index 2) the cavity is

$$\frac{dx}{ds} = \frac{m\frac{dx}{dt}}{m\frac{ds}{dt}} = \frac{p_x}{p_s}, \qquad \left.\frac{dx}{ds}\right|_2 = \left.\frac{m\frac{dx}{dt}}{m\frac{ds}{dt}}\right|_2 = \frac{p_{x,2}}{p_{s,2}}$$

Particle mass and velocity are modified at the traversal of the cavity but, as the

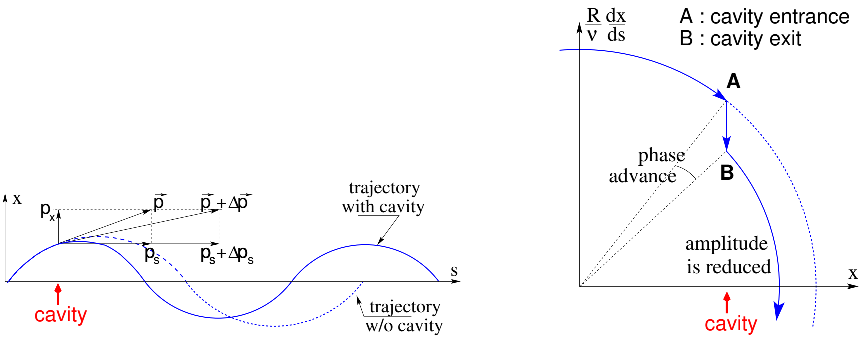

Fig. 9.14 Adiabatic damping of betatron oscillations, here from $x' = p_x/p_s$ before the cavity, to $x'_2 = p_x/(p_s + \Delta p_s)$ after the cavity. In the horizontal phase space, to the right, decrease of $\Delta\left(\frac{dx}{ds}\right)$ if $\frac{dx}{ds} > 0$, increase of $\Delta\left(\frac{dx}{ds}\right)$ if $\frac{dx}{ds} < 0$

force is longitudinal, $dp_x/dt = 0$ thus $p'_x = p_x$, the increase in momentum is purely longitudinal, $p'_s = p_s + \Delta p$. Thus

$$\left.\frac{dx}{ds}\right|_2 = \frac{p_x}{p_s + \Delta p} \approx \frac{p_x}{p_s}(1 - \frac{\Delta p}{p_s})$$

and as a consequence the slope dx/ds varies across the cavity,

$$\Delta\left(\frac{dx}{ds}\right) = \left.\frac{dx}{ds}\right|_2 - \frac{dx}{ds} = -\frac{dx}{ds}\frac{\Delta p_s}{p_s}$$

The variation of the slope is proportional to the slope, with opposite sign if $\Delta p/p > 0$ (acceleration) thus a decrease of the slope. This variation has two consequences on the betatron oscillation (Fig. 9.14):

- a change of the betatron phase,
- a modification of the betatron amplitude.

Coordinate transport

at the cavity writes $\begin{cases} x_2 = x \\ x_2' \approx \frac{p_x}{p_s}(1-\frac{dp}{p}) = x'(1-\frac{dp}{p}) \end{cases}$. In matrix form, $\begin{pmatrix} x_2 \\ x_2' \end{pmatrix} = [C]\begin{pmatrix} x \\ x' \end{pmatrix}$ with

$$[C] = \begin{bmatrix} 1 & 0 \\ 0 & 1-\frac{dp}{p} \end{bmatrix} \tag{9.30}$$

and $det[C] = 1 - \frac{dp}{p} \neq 1$: the system is non-conservative, the surface of the beam ellipse in phase space is not conserved. Assume one cavity in the ring and note $[T] \times [C]$ the one-turn coordinate transport matrix with origin at entrance of the cavity. Its determinant is $det[T] \times det[C] = det[C] = 1 - \frac{dp}{p}$; the variation of the transverse ellipse surface satisfies $\varepsilon_u = (1 - \frac{dp}{p_0})\varepsilon_0$ or, with $d\varepsilon_u = \varepsilon_u - \varepsilon_0$, $\frac{d\varepsilon_u}{\varepsilon_u} = -\frac{dp}{p_0}$, the solution of which is

$$p\ \varepsilon_u = constant, \quad or \quad \beta\gamma\varepsilon_u = constant \tag{9.31}$$

Over N turns the coordinate transport matrix is $[T_N] = ([T][C])^N$, its determinant is $(1-\frac{dp}{p})^N \approx 1 - N\frac{dp}{p}$: the ellipse surface changes by that factor.

Synchrotron motion; *phase stability*

"Synchrotron motion" designates the mechanism of phase stability, or longitudinal focusing (Fig. 9.15), that stabilizes the longitudinal motion of a particle in the vicinity of a synchronous phase, ϕ_s, in virtue of

(i) the presence of an accelerating cavity with its frequency indexed on the revolution time,

(ii) with the bunch centroid positioned either on the rising slope of the oscillating voltage (low energy regime), or on the falling slope (high energy regime).

The synchronous (or "ideal") particle follows the equilibrium trajectory around the ring (the reference closed orbit, about which all other particles will undergo a betatron oscillation), its velocity satisfies $v(t) = \frac{qB\rho(t)}{m}$; at each turn it reaches the accelerating gap when the oscillating voltage is at the synchronous phase ϕ_s, and undergoes an energy gain

$$\Delta W = q\hat{V}\sin\phi_s$$

The condition $|\sin\phi_s| < 1$ imposes a lower limit to the cavity voltage for acceleration to happen, namely, after Eq. 9.29,

$$\hat{V} > 2\pi R\rho\dot{B}$$

Referring to Fig. 9.15, the synchronous phase can be placed on the left (A A' A"... series in the Figure, or on the right (B B' B"... series) of the oscillating voltage crest.

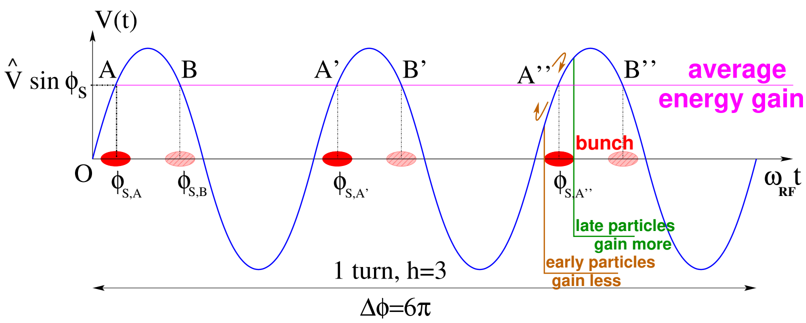

Fig. 9.15 A sketch of the mechanism of phase stability, $h = 3$ in this example. Below transition phase stability occurs for a synchronous phase taken at either one of A, A', A" arrival times at the gap: a particle with higher energy goes around the ring more rapidly than the synchronous particle; if both are launched together, the former arrives earlier at the voltage gap (at $\phi < \phi_{s,A}$) so experiencing weaker acceleration; at lower energy the particle is slower, it arrives at the gap later, $\phi > \phi_{s,A}$, so experiencing a greater voltage; this results in an overall stable oscillatory motion around the synchronous phase. Beyond transition the stable phase is at either one of B, B', B' locations: a particle which is less energetic than the synchronous particle arrives earlier, $\phi < \phi_{s,B}$, so experiencing a greater voltage, and inversely, resulting in overall stable synchrotron motion.

One and only one of these two possibilities, and which one depending upon the optical lattice and on particle energy, ensures that particles in a bunch remain grouped in the vicinity of the synchronous particle. The transition is between two time-of-flight regimes: a particle which gains momentum compared to the synchronous particle has a greater velocity, while

- in the high bunch energy regime the increase in path length around the ring is faster than the increase in velocity (velocity essentially does not even change in ultrarelativistic regime), a revolution around the ring takes more time (this is the classical cyclotron and synchrocyclotron regime, and as well the high energy electron synchrotron regime); consider such a particle, arriving at the accelerating gap late ($\phi(t) > \phi_s$), in order for it to be pulled toward bunch center (*i.e.*, take less time around the ring) it has to undergo deceleration; this is the B series, above transition;

- in the low bunch energy regime velocity increase is faster than path length increase, thus a revolution around the ring is faster; consider such a particle, arriving at the accelerating gap early ($\phi(t) < \phi_s$), in order for it to be pulled toward bunch center (*i.e.*, take more time around the ring) it has to be slowed down, it has to undergo deceleration; this is the A series, below transition.

Transition energy

The transition between the two time-of-flight regimes occurs at $\frac{dT_{\mathrm{rev}}}{T_{\mathrm{rev}}} = 0$. With $T = 2\pi/\omega = C/v$, this can be written $\frac{d\omega_{\mathrm{rev}}}{\omega_{\mathrm{rev}}} = -\frac{dT_{\mathrm{rev}}}{T_{\mathrm{rev}}} = \frac{dv}{v} - \frac{dC}{C}$. With $\frac{dv}{v} = \frac{1}{\gamma^2}\frac{dp}{p}$

and momentum compaction $\alpha = \dfrac{dC}{C} \,/\, \frac{dp}{p}$, (Eq. 9.28), this can be written

$$\frac{d\omega_{\text{rev}}}{\omega_{\text{rev}}} = -\frac{dT_{\text{rev}}}{T_{\text{rev}}} = \left(\frac{1}{\gamma^2} - \alpha\right)\frac{dp}{p} = \eta\frac{dp}{p} \tag{9.32}$$

wherein the phase-slip factor has been introduced,

$$\eta = \overbrace{\frac{1}{\gamma^2}}^{\text{kinematics}} - \underbrace{\alpha}_{\text{lattice}} = \frac{1}{\gamma^2} - \frac{1}{\gamma_{\text{tr}}^2} \tag{9.33}$$

The transition γ appears to be a property of the lattice.

In a weak focusing lattice $\gamma_{\text{tr}} = 1/\sqrt{\alpha} \approx \nu_x$ (Eqs. 4.21, 9.28), thus the phase stability regime is

$$\begin{aligned} &\text{below transition, } \textit{i.e. } \phi_s < \pi/2, \quad \text{if} \quad \gamma < \nu_x \\ &\text{above transition, } \textit{i.e.} \phi_s > \pi/2, \quad \text{if} \quad \gamma > \nu_x \end{aligned} \tag{9.34}$$

In a weak focusing synchrotron the horizontal tune $\nu_x = \sqrt{(1-n)R/\rho_0}$ (Eq. 9.23) may be $\gtrless 1$, and subsequently $\gamma_{\text{tr}} > 1$ is a possibility. There is no transition-gamma if $\nu_x < 1$. Acceleration to 3 GeV in SATURNE I for instance, from 50 MeV at injection, and with $\nu_x \approx 0.7$ (Tab. 9.1) did not require transition-gamma crossing[3].

9.1.3 Depolarizing Resonances

The field index is essentially zero in the ZGS, transverse focusing is ensured by wedge angles at the ends of the height dipoles, the only location where non-zero radial field components are found. The latter are weak anyway, as a consequence so are depolarizing resonances: *"As we can see from the table, the transition probability [from spin state $\psi_{1/2}$ to spin state $\psi_{-1/2}$] is reasonably small up to $\gamma = 7.1$"* [12], *i.e.* $G\gamma = 12.73$, $p = 6.6$ GeV/c; the table referred to stipulates a transition probability $P_{\frac{1}{2},-\frac{1}{2}} < 0.042$, whereas resonances beyond that energy range feature $P_{\frac{1}{2},-\frac{1}{2}} > 0.36$. Beam depolarization up to 6 GeV/c, under the effect of these resonances, is illustrated in Fig. 9.16.

In a synchrotron using gradient dipoles, particles experience radial fields all along the latter as they undergo vertical betatron oscillations, as an effect of the radial field index [12, 20, 21]. However these radial field components are weak, and so is there

[3] Transition-gamma crossing, or "gamma jump", is a common beam manipulation during acceleration in strong focusing synchrotrons, it requires an RF phase jump, the technique is addressed in Chapter 10.

effect on spin motion as long as the particle energy is low enough (an effect of the γ factor in the spin precession Eq. 4.29, Chap. 4).

Assuming a defect-free ring, the vertical betatron motion excites "intrinsic" spin resonances, located at

$$G\gamma_R = k\,P \pm \nu_y$$

with k an integer and P the period of the ring. In the ZGS for instance, $\nu_y \approx 0.8$ (Tab. 9.2), the ring is P=4-periodic, thus $G\gamma_R = 4k \pm 0.8$. Strongest resonances are located at

$$G\gamma_R = mk\,P \pm \nu_y$$

with m the number of cells per superperiod [22, Sec. 3.II]. In the ZGS, m=2 thus strongest resonances occur at $G\gamma_R = 2 \times 4k \pm 0.8 = 7.2$ ($p = 3.65$ GeV/c), 8.8 (4.51 GeV/c), 15.2 (7.9 GeV/c), ... (Fig. 9.16).

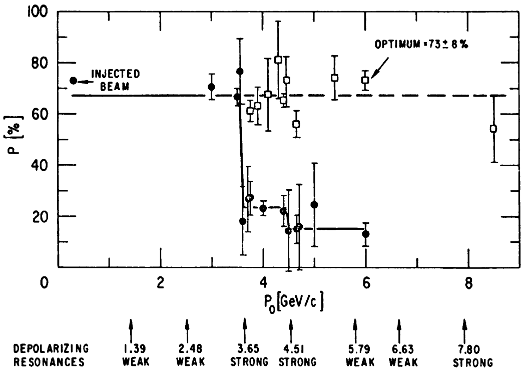

Fig. 9.16 Depolarizing intrinsic resonance landscape up to 9 GeV/c at the ZGS (solid circles) [23]. Systematic resonances are located at $G\gamma_R = 4 \times \text{integer} \pm \nu_y$, stronger ones at $G\gamma_R = 8 \times \text{integer} \pm \nu_y$. A tune jump was applied to preserve polarization when crossing strong resonances (empty circles)

In the presence of vertical orbit defects, non-zero periodic transverse fields are experienced along the closed orbit, they excite "imperfection" depolarizing resonances, located at

$$G\gamma_R = k$$

with k an integer. In the case of systematic defects the periodicity of the orbit is that of the lattice, P, imperfection resonances are located at $G\gamma_R = kP$. Strongest imperfection resonances are located at [22, Sec. 3.II]

$$G\gamma_R = mk\,P$$

Crossing a depolarizing resonance of strength ϵ_R causes a loss of polarization given by (Froissart-Stora formula [24])

$$\frac{P_f}{P_i} = 2e^{-\frac{\pi}{2}\frac{|\epsilon_R|^2}{\alpha}} - 1 \qquad (9.35)$$

from a value P_i upstream to an asymptotic value P_f downstream of the resonance. This assumes an isolated resonance, crossed at an energy gain ΔE per turn, with a crossing speed

$$\alpha = G\frac{d\gamma}{d\theta} = \frac{1}{2\pi}\frac{\Delta E}{M} \tag{9.36}$$

Spin precession axis. Resonance width

Consider the spin vector $\mathbf{S}(\theta) = (S_\eta, S_\xi, S_y)$ of a particle in the laboratory frame, with θ the orbital angle around the accelerator. Introduce the projection $s(\theta)$ of $\mathbf{S}$ in the median plane

$$s(\theta) = S_\eta(\theta) + jS_\xi(\theta) \qquad (\text{and } \ S_y^2 = 1 - s^2) \tag{9.37}$$

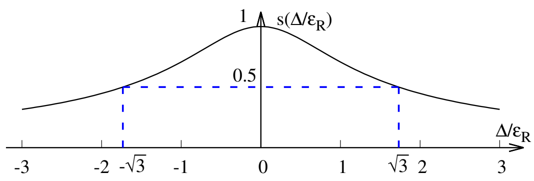

Fig. 9.17 Modulus of the horizontal spin component. $s = 1/2$ at distance $\Delta = \pm\sqrt{3}\epsilon_R$ from $G\gamma_R$

It can be shown that in the case of a stationary solution of the spin motion, viz. the spin precession axis, s satisfies [21] (Fig. 9.17)

$$s^2 = \frac{1}{1 + \dfrac{\Delta^2}{|\epsilon_R|^2}} \tag{9.38}$$

with $\Delta = G\gamma - G\gamma_R$ the distance to the resonance. The resonance width is a measure of its strength (Fig. 9.18). The quantity of interest is the angle, ϕ, of the spin precession direction to the vertical axis, given by (Fig. 9.18)

$$\cos\phi(\Delta) \ \equiv S_y(\Delta) = \sqrt{1 - s^2} = \frac{\Delta/|\epsilon_R|}{\sqrt{1 + \Delta^2/|\epsilon_R|^2}} \tag{9.39}$$

On the resonance, $\Delta = 0$, the spin precession axis lies in the bend plane: $\phi = \pm\pi/2$. $S_y = 0.99$ (1% depolarization) corresponds to a distance to the resonance $\Delta = 7|\epsilon_R|$, spin precession axis at an angle $\phi = \mathrm{acos}(0.99) = 8^o$ from the vertical.

Conversely, given S_y,

$$\frac{\Delta^2}{|\epsilon_R|^2} = \frac{S_y^2}{1 - S_y^2} \tag{9.40}$$

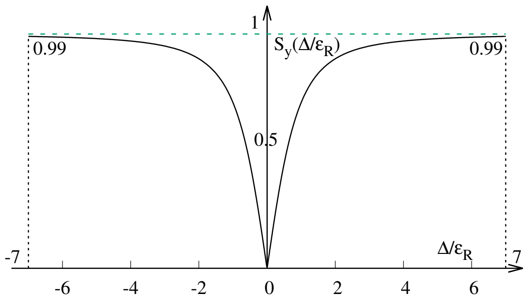

Fig. 9.18 Dependence of polarization on the distance to the resonance. For instance $S_y = 0.99$, 1% depolarization, corresponds to $\Delta = 7|\epsilon_R|$. On the resonance, $\Delta = 0$, the precession axis lies in the median plane, $S_y = 0$

The precession axis is common to all spins, S_y is a measure of the polarization along the vertical axis,

$$S_y = \frac{N^+ - N^-}{N^+ + N^-}$$

wherein N^+ and N^- denote the number of particles in spin states $\frac{1}{2}$ and $-\frac{1}{2}$ respectively.

Spin motion through weak resonances

Depolarizing resonances are weak up to several GeV in a weak focusing synchrotron, as the radial and/or longitudinal fields, which stem from a small radial field index and from dipole fringe fields, are weak. Spin motion $S_y(\theta)$ through a resonance in that case can be assumed to satisfy $S_{y,f} \approx S_{y,i}$, with $S_{y,f}$ and $S_{y,i}$ the asymptotic vertical spin component values respectively upstream and downstream of the resonance). As a consequence it can be calculated in terms of the Fresnel integrals [20, 21]

$$C(x) = \int_0^x \cos\left(\frac{\pi}{2}t^2\right)\,dt, \qquad S(x) = \int_0^x \sin\left(\frac{\pi}{2}t^2\right)\,dt$$

namely, with the origin of the orbital angle is taken at the resonance (Fig. 9.19),

$$\begin{aligned} if\ \theta < 0:\ \left(\frac{S_y(\theta)}{S_{y,i}}\right)^2 &= 1 - \frac{\pi}{\alpha}|\epsilon_R|^2 \left\{\left[0.5 - C\left(-\theta\sqrt{\frac{\alpha}{\pi}}\right)\right]^2 + \left[0.5 - S\left(-\theta\sqrt{\frac{\alpha}{\pi}}\right)\right]^2\right\} \\ if\ \theta > 0:\ \left(\frac{S_y(\theta)}{S_{y,i}}\right)^2 &= 1 - \frac{\pi}{\alpha}|\epsilon_R|^2 \left\{\left[0.5 + C\left(\theta\sqrt{\frac{\alpha}{\pi}}\right)\right]^2 + \left[0.5 + S\left(\theta\sqrt{\frac{\alpha}{\pi}}\right)\right]^2\right\} \end{aligned} \tag{9.41}$$

In the asymptotic limit,

$$\frac{S_y(\theta)}{S_{y,i}} \xrightarrow{\theta\to\infty} 1 - \frac{\pi}{\alpha}|\epsilon_R|^2 \tag{9.42}$$

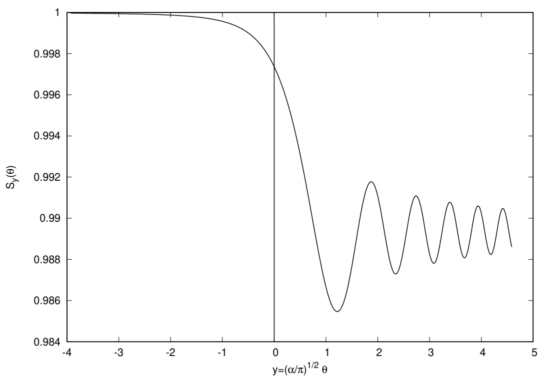

Fig. 9.19 Vertical component of spin motion $S_y(\theta)$ through a weak depolarizing resonance (after Eq. 9.41). The vertical bar is at the location of the resonance, which coincides with the origin of the orbital angle

which identifies with the development of Froissart-Stora formula $P_f/P_i = 2\exp(-\frac{\pi}{2}\frac{|\epsilon_R|^2}{\alpha}) - 1$ to the first order in $|\epsilon_R|^2/\alpha$. This approximation holds in the limit that higher order terms can be neglected: $|\epsilon_R|^2/\alpha \ll 1$.

9.2 Exercises

9.1 Construct SATURNE I (weak index) synchrotron. Spin Resonances
Solution: page 304

In this exercise, SATURNE I weak focusing 3 GeV synchrotron is modeled. Spin resonances in a weak dipole gradient lattice are studied.

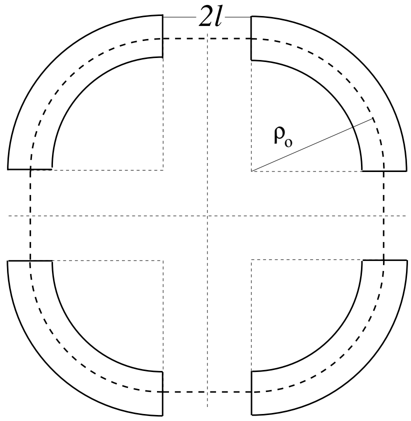

Fig. 9.20 A schematic layout of SATURNE I, a $2\pi/4$ axial symmetry structure, comprised of 4 radial field index 90 deg dipoles and 4 drift spaces. The cell in the simulation exercises is taken as a $\pi/4$ quadrant: l-drift/90^o-dipole/l-drift

Table 9.1 Parameters of SATURNE I weak focusing synchrotron [25]. ρ_0 denotes the reference bending radius in the dipole; the reference orbit, field index, wave numbers, etc., are taken along that radius

Orbit length, C	cm	6890
Average radius, $R = C/2\pi$	cm	1096.58
Straight section length. $2l$	cm	400
Magnetic radius, ρ_0	cm	841.93
R/ρ_0		1.30246
Field index n, nominal value		0.6
Wave numbers, ν_x; ν_y		0.724; 0.889 **** verif wrt. simuls
Stability limit		$0.5 < n < 0.757$
Injection energy	MeV	3.6
Field at injection	kG	0.326
Top energy	GeV	2.94
$\dot{B}$	kG/s	18
Field at top energy, $B_{\max}$	kG	14.9
$B_{\max}\rho$	T m	13
Field ramp at injection	kG/s	20
Synchronous energy gain	keV/turn	1.160
RF harmonic		2

(a) Construct a model of SATURNE I 90^o cell dipole in the hard-edge model, using DIPOLE. Use the parameters given in Tab. 9.1, and Fig. 10.7 as a guidance. In order to allow beam monitoring, split the dipole in two 45^odeg halves. It is judicious to take RM=841.93 cm in DIPOLE, as this is the reference radius for the definition of the radial index. Take an integration step size in centimeter range - small enough to ensure numerical convergence, as large as doable for fast multiturn raytracing.

Validate the model by producing the 6×6 transport matrix of the cell dipole (MATRIX[IFOC=0] can be used for that, with OBJET[KOBJ=5] to define a proper set of paraxial initial coordinates) and checking against theory (Sect. 15.2, Eq. 15.6).

(b) Construct a model of SATURNE I cell, with origin at the center of the drift. Find the closed orbit, that particular trajectory which has all its coordinates zero in the drifts: use DIPOLE[KPOS] to cancel the closed orbit coordinates at DIPOLE ends. While there, check the expected value of the dispersion (Eq. 9.26) and of the momentum compaction (Eq. 9.28), from the raytracing of a chromatic closed orbit - *i.e.*, the orbit of an off-momentum particle. Plot these two orbits (on- and off-momentum), over a complete turn around the ring, on a common graph.

Compute the cell periodic optical functions and tunes, using either MATRIX[IFOC=11] or TWISS; check their values against theory. Check consistency with previous dispersion function and momentum compaction outcomes.

Move the origin of the lattice at a different azimuth s along the cell: verify that, while the transport matrix depends on the origin, its trace does not.

Produce a graph of the optical functions (betatron functions and dispersion) along the cell. Check the expected average values of the betatron functions (Eq. 9.20).

Produce a scan of the tunes over the field index range $0.5 \le n \le 0.757$. REBELOTE can be used to repeatedly change n over that range. Superimpose the theoretical curves $\nu_x(n)$, $\nu_y(n)$.

(c) Justify considering the betatron oscillation as sinusoidal, namely,

$$y(\theta) = A\,\cos(\nu_y\theta + \phi)$$

wherein $\theta = s/R$, $R = \oint ds/2\pi$.

(d) Launch a few particles evenly distributed on a common paraxial horizontal Courant-Snyder invariant, vertical motion taken null (OBJET[KOBJ=8] can be used), for a single pass through the cell. Store particle data along the cell in zgoubi.plt, using DIPOLE[IL=2] and DRIFT[split,N=20,IL=2]. Use these to generate a graph of the beam envelopes.

Using Eq. 9.22 compare with the results obtained in (b). Find the minimum and maximum values of the betatron functions, and their azimuth $s(min[\beta_x])$, $s(max[\beta_x])$. Check the latter against theory.

Repeat for the vertical motion, taking $\varepsilon_x = 0$, ε_y paraxial.

Repeat, using, instead of several particles on a common invariant, a single particle traced over a few tens of turns.

(e) Produce an acceleration cycle from 3.6 MeV to 3 GeV, for a few particles launched on a common $10^{-4}\,\pi$m initial invariant in each plane. Ignore synchrotron motion (CAVITE[IOPT=3] can be used in that case). Take a peak voltage $\hat{V} = 200$ kV (unrealistic though, as it would result in a nonphysical $\dot{B}$ (Eq. 9.29)) and synchronous phase $\phi_s = 150$ deg (justify $\phi_s > \pi/2$).

Check the betatron damping over the acceleration range: compare with theory (Eq. 9.31).

How close to symplectic the numerical integration is (it is by definition *not* symplectic, being a truncated Taylor series method [26, Eq. 1.2.4]), depends on the integration step size, and on the size of the flying mesh in the DIPOLE method [26, Fig. 20]; check a possible departure of the betatron damping from theory as a function of these parameters.

Produce a graph of the horizontal and vertical wave number values over the acceleration cycle.

(f) Some spin motion, now. Adding SPNTRK at the beginning of the sequence will ensure spin tracking.

Based on the file worked out for question (d), simulate the acceleration of a single particle, through the intrinsic resonance $G\gamma_R = 4 - \nu_Z$, from a few thousand turns upstream to a few thousand turns downstream. On a common graph, plot $S_y(turn)$ for a few different values of the vertical betatron invariant (the horizontal invariant value does not matter - explain that statement, it can be taken zero).

(g) Produce a graph of the average value of S_Z over a 200 particle set, as a function of $G\gamma$, across the $G\gamma_R = 4 - \nu_Z$ resonance. Indicate on that graph the location of the resonant $G\gamma_R$ values.

Perform this resonance crossing for five different values of the particle invariant: $\varepsilon_Z/\pi = 2,\ 10,\ 20,\ 40,\ 200\,\mu$m. Compute P_f/P_i in each case, check the dependence on ε_Z against theory.

Compute the resonance strength, ε_Z, from these trackings.

Re-do this crossing simulation for a different crossing speed (take for instance $\hat{V} = 10\,\mathrm{kV}$) and a couple of vertical invariant values, compute P_f/P_i so obtained. Check the crossing speed dependence of P_f/P_i against theory.

(h) Show that the previous weak resonance crossings ($P_f/P_i \approx 1$) satisfies Eq. 9.41. Match the tracking data to the latter to get the vertical betatron tune ν_y, the location of the resonance $G\gamma_\mathrm{R}$, and its strength.

(i) Track a few particles at fixed energy, at distances from the resonance $G\gamma_R = 4 - \nu_y$ of up to a $7 \times \epsilon_R$ (this distance corresponds to 1% depolarization).

Produce on a common graph the spin motion $S_Z(turn)$ for all these particles, as observed at some azimuth along the ring.

Produce a graph of $\langle S_y \rangle|_\mathrm{turn}(\Delta)$ (as in Fig. 9.18).

Produce the vertical betatron tune ν_y, the location of the resonance $G\gamma_\mathrm{R}$, and its strength, obtained from a match of these tracking trials to (Eq. 9.39)

$$\langle S_y \rangle (\Delta) = \frac{\Delta}{\sqrt{|\epsilon_R|^2 + \Delta^2}}$$

9.2 Construct the ZGS (zero-gradient) synchrotron. Spin Resonances
Solution: page 328

In this exercise, the ZGS 12 GeV synchrotron is modeled. Spin resonances in a zero-gradient, wedge focusing synchrotron are studied.

A photo taken in the ZGS tunnel is given in Fig. 9.4; a schematic layout of the ring is shown in Fig. 9.21, and a sketch of the double dipole cell in Fig. 9.22. Table 9.2 details the parameters of the synchrotron resorted to in these simulations.

(a) Construct a model of ZGS 45^o cell dipole in the hard-edge model, using DIPOLE. Use the parameters given in Tab. 9.2, and Figs. 9.21, 9.22 as a guidance. In order to allow beam monitoring, split the dipole in two 22.5^odeg halves. Take the closed orbit radius as the reference RM=2076 cm in DIPOLE: it will be assumed that the orbit is the same at all energies[4]. Take an integration step size in centimeter range - small enough to ensure numerical convergence, as large as doable for fast multiturn raytracing.

Validate the model by producing the 6×6 transport matrices of both dipole (MATRIX[IFOC=0] can be used for that, with OBJET[KOBJ=5] to define a proper set of paraxial initial coordinates) and checking against theory (Sect. 15.2, Eq. 15.6).

Add fringe fields in DIPOLE[λ,$C_0 - C_5$], the rest if the exercise will use that model. Take fringe field extent and coefficient values

$$\lambda = 60\,\mathrm{cm}\ C_0 = 0.1455,\ C_1 = 2.2670,\ C_2 = -0.6395,\ C_3 = 1.1558,\ C_4 = C_5 = 0 \tag{9.43}$$

($C_0 - C_5$ determine the shape of the field fall-off, they have been computed from a typical measured field profile $B(s)$).

[4] Note that in reality the reference orbit in ZGS moved outward during acceleration [27].

(b) Construct a model of ZGS cell accounting for dipole fringe fields, with origin at the center of the long drift. In doing so, use DIPOLE[KPOS] to cancel the closed orbit coordinates at DIPOLE ends.

Compute the periodic optical functions at cell ends, and cell tunes, using MATRIX[IFOC=11]; check their values against theory.

Move the origin at the location (azimuth s along the cell) of the betatron functions extrema: verify that, while the transport matrix depends on the origin, its trace does not. Verify that the local betatron function extrema, and the dispersion function, have the expected values.

Produce a graph of the optical functions (betatron functions and dispersion) along the cell.

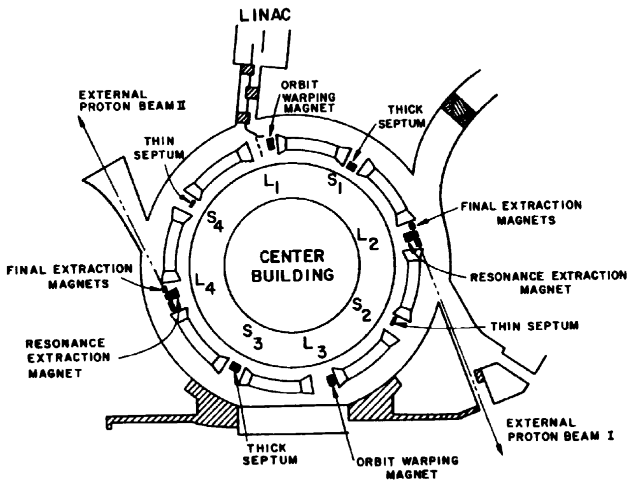

Fig. 9.21 A schematic layout of the ZGS [23], a $\pi/2$-periodic structure, comprised of 8 zero-index dipoles, 4 long and 4 short straight sections

(c) Additional verifications regarding the model.

Produce a graph of the field B(s)

- along the on-momentum closed orbit, and along off-momentum chromatic closed orbits, across a cell;

- along orbits at large horizontal excursion;

- along orbits at large vertical excursion.

For all these cases, verify qualitatively, from the graphs, that $B(s)$ appears as expected.

(d) Justify considering the betatron oscillation as sinusoidal, namely,

$$y(\theta) = A\ \cos(\nu_y \theta + \phi)$$

wherein $\theta = s/R$, $R = \oint ds/2\pi$.

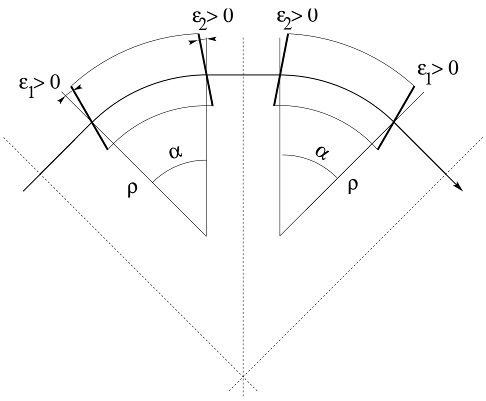

Fig. 9.22 A sketch of ZGS cell layout. In defining the entrance and exit faces (EFBs) of the magnet, beam goes from left to right. Wedge angles at the long straight sections (ε_1) and at the short straight sections (ε_2) are different

Table 9.2 Parameters of the ZGS weak focusing synchrotron after Refs. [27, 28] [23, pp. 288-294,p. 716] (2nd column, when they are known) and in the present simplified model and numerical simulations (3rd column). Note that the actual orbit moves during ZGS acceleration cycle, tunes change as well - this is not taken into account in the present modeling, for simplicity

		From Refs. [27, 28]	**Simplified model**
Injection energy	MeV	50	
Top energy	GeV	12.5	
$G\gamma$ span		1.888387 - 25.67781	
Length of central orbit	m	171.8	170.90457
Length of straight sections, total	m	41.45	40.44
Lattice			
Wave numbers ν_x; ν_y		0.82; 0.79	0.849; 0.771
Max. β_x; β_y	m		32.5; 37.1
Magnet			
Length	m	16.3	16.30486 (magnetic)
Magnetic radius	m	21.716	20.76
Field min.; max.	kG	0.482; 21.5	0.4986; 21.54
Field index		0	
Yoke angular extent	deg	43.02590	45
Wedge angle	deg	≈10	13 and 8
RF			
Rev. frequency	MHz	0.55 - 1.75	0.551 - 1.751
RF harmonic h=$\omega_{\mathrm{rf}}/\omega_{\mathrm{rev}}$		8	
Peak voltage	kV	20	200
B-dot, nominal/max.	T/s	2.15/2.6	
Energy gain, nominal/max.	keV/turn	8.3/10	100
Synchronous phase, nominal	deg	150	
Beam			
ε_x; ε_y (at injection)	$\pi\mu$m	25; 150	
Momentum spread, rms		3×10^{-4}	
Polarization at injection	%	>75	100
Radial width of beam (90%), at inj.	inch	2.5	$\sqrt{\beta_x\varepsilon_x/\pi}$ = 1.1

(e) Produce an acceleration cycle from 50 MeV to 17 GeV about, for a few particles launched on a common $10^{-5}\,\pi$m vertical initial invariant, with small horizontal invariant. Ignore synchrotron motion (CAVITE[IOPT=3] can be used in that case). Take a peak voltage $\hat{V} = 200\,$kV (this is unrealistic but yields 10 times faster computing than the actual $\hat{V} = 20\,$kV, Tab. 9.2) and synchronous phase $\phi_s = 150\,$deg (justify $\phi_s > \pi/2$). Add spin, using SPNTRK, in view of the next question, (f).

Check the accuracy of the betatron damping over the acceleration range, compared to theory. How close to symplectic the numerical integration is (it is by definition *not* symplectic), depends on the integration step size, and on the size of the flying mesh in the DIPOLE method [26, Fig. 20]; check a possible departure of the betatron damping from theory as a function of these parameters.

Produce a graph of the evolution of the horizontal and vertical wave numbers during the acceleration cycle.

(f) Using the raytracing material developed in (e): produce a graph of the vertical spin component of the particles, and the average value over that 200 particle set, as a function of $G\gamma$. Indicate on that graph the location of the resonant $G\gamma_R$ values.

(g) Based on the simulation file used in (f), simulate the acceleration of a single particle, through one particular intrinsic resonance, from a few thousand turns upstream to a few thousand turns downstream.

Perform this resonance crossing for different values of the particle invariant. Determine the dependence of final/initial vertical spin component value, on the invariant value; check against theory.

Re-do this crossing simulation for a different crossing speed. Check the crossing speed dependence of final/initial vertical spin component so obtained, against theory.

(h) Introduce a vertical orbit defect in the ZGS ring.

Find the closed orbit.

Accelerate a particle launched on that closed orbit, from 50 MeV to 17 GeV about, produce a graph of the vertical spin component.

Select one particular resonance, reproduce the two methods of (g) to check the location of the resonance at $G\gamma_R$ =integer, and to find its strength.

References

1. Veksler, V.: A new method of acceleration of relativistic particles. J. of Phys. USSR 9 153-158 (1945)
2. McMillan, E. M.: The Synchrotron. Phys. Rev. 68 143-144 (1945)
3. Goward, F. K., and Barnes, D. E.: Experimental 8 MeV synchrotron for electron acceleration. Nature 158, 413 (1946)
4. Richardson, J.R., et al.: Frequency Modulated Cyclotron. Phys. Rev. 69: 669 (1946)
5. Kerst, D. W.: The Acceleration of Electrons by Magnetic Induction.. Phys. Rev., 60, 47-53 (1941)
6. SATURNE I photos: FAR_SA_N_00248, FAR_SA_N_02826; credit CEA Saclay. Archives historiques CEA. Copyright CEA/Service de documentation
7. Sessler, A., Wilson, E.: Engines of Discovery. A Century of Particle Accelerators. World Scientific, 2007
8. Fig. 9.3: Credit Reider Hahn, Fermilab
9. Endo, K., et al.: Compact proton and carbon ion synchrotrons for radiation therapy. MOPRI087, Proceedings of EPAC 2002, Paris, France; pp. 2733-2735. https://accelconf.web.cern.ch/e02/PAPERS/MOPRI087.pdf
10. Vostrikov, V.A., et al.: Novel approach to design of the compact proton synchrotron magnetic lattice. tupsa17, 26th Russian Particle Accelerator Conference RUPAC2018, Protvino, Russia (2018). https://accelconf.web.cern.ch/rupac2018/papers/tupsa17.pdf
11. Cohen, D, : Feasibility of Accelerating Polarized Protons with the Argonne ZGS. Review of Scientific Instruments 33, 161 (1962).// https://doi.org/10.1063/1.1746524
12. Ratner, L.G. and Khoe, T.K.: Acceleration of Polarized Protons in the Zero Gradient Synchrotron. Procs. PAC 1973 Conference, Washington (1973). http://accelconf.web.cern.ch/p73/PDF/PAC1973_0217.PDF
13. Bywatwr, J., Khoe, T., et al.: A pulsed quadrupole system for preventing depolarization. IEEE Transactions on Nuclear Science (Volume: 20, Issue: 3, June 1973)
14. Cho, Y., et als.: Effects of depolarizing resonances on a circulating beam of polarized protons during or storage in a synchrotron. IEEE Trans. Nuclear Science, Vol.NS-24, No.3, June 1977
15. Parker, E.F.: High Energy Polarized Deuterons at the Argonne National Laboratory Zero Gradient Synchrotron. IEEE Transactions on Nuclear Science, Vol. NS-26, No. 3, June 1979, pp 3200-3202

16. Leleux, G.: Accélérateurs Circulaires. Lecture Notes, INSTN, CEA Saclay (1978)
17. Suddeth, D.E., et als.: Pole face winding equipment for eddy current correction at the Zero Gradient Synchrotron. Procs. PAC 1973 Conference, Washington (1973). http://accelconf.web.cern.ch/p73/PDF/PAC1973_0397.PDF
18. Rauchas, A.V. and Wright, A.J.: Betatron tune profile control in the Zero Gradient Synchrotron (ZGS) using the main magnet pole face windings. Procs. PAC1977 conference, IEEE Trans. on Nucl. Science, VoL.NS-24, No.3, June 1977
19. Floquet, G.: Sur les équations différentielles linéaires à coefficients périodiques. Annales scientifiques de l'E.N.S. 2e série, tome 12 (1883), p. 47-88. http://www.numdam.org/item?id=ASENS_1883_2_12__47_0
20. Leleux, G.: Traversée des résonances de dépolarisation. Rapport Interne LNS/GT-91-15, SATURNE, Groupe Théorie, CEA Saclay (février 1991)
21. Méot, F.: Spin Dynamics. Polarized Beam Dynamics and Instrumentation in Particle Accelerators, USPAS Summer 2021 Spin Class proceedings, Springer (2023)
22. Lee, S.Y.: Spin Dynamics and Snakes in Synchrotrons. World Scientific, 1997
23. Khoe, T.K., et al.: The High Energy Polarized Beam at the ZGS. Procs. IXth Int. Conf on High Energy Accelerators, Dubna, pp. 288-294 (1974).
24. Froissart, M. and Stora, R.: Dépolarisation d'un faisceau de protons polarisés dans un synchrotron. Nucl. lnst. Meth. 7 (l960) 297.
25. Bruck H., Debraine P., Levy-Mandel R., Lutz J., Podliasky I., Prevot F., Taieb J., Winter S.D., Maillet R., Caractéristiques principales du Synchrotron à Protons de Saclay et résultats obtenus lors de la mise en route, rapport CEA no.93, CEN-Saclay, 1958.
26. Méot, F.: Zgoubi Users' Guide. https://www.osti.gov/biblio/1062013-zgoubi-users-guide Sourceforge latest version: https://sourceforge.net/p/zgoubi/code/HEAD/tree/trunk/guide/Zgoubi.pdf
27. Foss, M.H., et al.: The Argonne ZGS Magnet. IEEE 1965, pp. 377-382, June 1965
28. Klaisner, L.A., et al.: IEEE 1965, pp. 133-137, June 1965